Supplementary Materials

Chlamydomonas-Inspired Water-Air Interface Mini-Robot with Intricate Tectonics, Programmable Locomotion, and Multifunctional Execution

Lihuang Li,[1,6,#] Libing Huang,[1,#] Wenyi Liao,[1] Guangshan Wang,[3] Hao Sun,[4,5]* Lei Ren,[1,2,7]* Miao Wang[1,7]*

[1]The Higher Educational Key Laboratory for Biomedical Engineering of Fujian Province, Research Center of Biomedical Engineering of Xiamen, Department of Biomaterials, College of Materials, Xiamen University, Xiamen 361005, China.

[2]State Key Lab of Physical Chemistry of Solid Surfaces, Xiamen University, Xiamen 361005, China.

[3]Department of Mechanical and Energy Engineering, Southern University of Science and Technology, Shenzhen 518055, China.

[4]State Key Laboratory of Robotics and System, Harbin Institute of Technology, Harbin 150001, China.

[5]Research Center of Aerospace Mechanism and Control, School of Mechatronics Engineering, Harbin Institute of Technology, Harbin 150001, China.

[6]School of Mechanical Engineering and Automation, Fuzhou University, Fuzhou 350116, China.

[7]State Key Laboratory of Vaccines for Infectious Diseases, Xiang An Biomedicine Laboratory, Xiamen 361005, China.

[#]These authors contribute equally to this work.

*Corresponding author: Lei Ren, E-mail: renlei@xmu.edu.cn; Hao Sun, E-mail: sunnice@hit.edu.cn; Miao Wang, Email: miaowang@xmu.edu.cn.

The supplementary materials file includes:

Text.

Fig. S1-S28.

Movie S1-S7. (mp4 format).

Text

Derivation of the relationship between fuel release rate and velocity of motion

The rate of fuel release can be expressed in terms of flux (J), which is described by following equation [1,2]:

$$J=-D\cdot \mathrm{d}C/\mathrm{d}x=v_e\cdot\rho_e \tag{S1}$$

Where v_e is the velocity of the fuel at the channel exit, and ρ_e is the density of the fuel.

As we know, the momentum of the robot is equal to the impulse of the external force. In addition, if the heat transmission was ignored, the momentum of the robot is equal to the momentum of the fuel in whole system, that is to say, the acceleration of robot results from the consumption of fuel in the system itself. This process can be written as:

$$(F_m-f)\mathrm{d}t=m\mathrm{d}v=v_e\cdot\mathrm{d}m \tag{S2}$$

Where F_m is the force producing by the Marangoni effect, f is the friction of the robot, t for time, v is the velocity of the robot, and m is the mass of the system. Furthermore, F_m and the f could be described by following equation:

$$F_m=L(\gamma_s-\gamma_f) \tag{S3}$$

$$f=kv^n \tag{S4}$$

Where L is the length of the effective surface tension acting, γ_s and γ_f are the surface tensions of solution and the fuel, and k is the friction coefficient. According to equations (S1)-(S4), the relationship between J and v can be deduced as follows:

$$J=\rho_e\cdot(L\cdot\Delta\gamma-kv^n)\mathrm{d}t/\mathrm{d}m \tag{S5}$$

Morphology and locomotion behavior of Chlamydomonas

Chlamydomonas, a kind of unicellular green alga living in ponds, has an oval body with major axis of 7.91±0.96 μm and minor axis of 6.40±0.90 μm, and two flagellum with lengths of 10.38±1.31 μm and diameter of 0.26±0.04 μm on the head (Fig. S1). The complex locomotion behavior of Chlamydomonas could be divided into rotational and straight (Fig. 2A). For rotational behavior, the flagellum of Chlamydomonas beats with different phases and orientation. The unbalanced beating efficiency caused Chlamydomonas to produce a total tug force (F_{Cr}), which application point away from the center of the body. For straight behavior, the flagellum of Chlamydomonas beat with synchronous phase and orientation. The symmetric beating efficiency caused Chlamydomonas to produce a total tug force (F_{Cs}), which application point locate in the center of body. With the complex coupling of straight and rotation[3], the Chlamydomonas can exhibit abundance of modalities in swimming behavior that enables them to adapt to the complex physical environment (Fig. S2A Movie S1). In order to further quantitative analyses the total tug force, we translated the behavioral analysis of Chlamydomonas into the spatiotemporal evolution of Chlamydomonas positions (Fig. S2B). The kinematics characteristics of Chlamydomonas can be described with the measured body center coordinates and angular displacements (X_i, Y_i, θ_i):

$$v_x = \frac{\mathrm{d}X_i}{\mathrm{d}t}\cos\theta_i + \frac{\mathrm{d}Y_i}{\mathrm{d}t}\sin\theta_i \tag{S6}$$

$$v_y = -\frac{\mathrm{d}X_i}{\mathrm{d}t}\sin\theta_i + \frac{\mathrm{d}Y_i}{\mathrm{d}t}\cos\theta_i \tag{S7}$$

$$\omega = \frac{\mathrm{d}\theta_i}{\mathrm{d}t} \tag{S8}$$

Where v_x is the component of Chlamydomonas velocity in the direction of the major axis, v_y is the component of Chlamydomonas velocity in the direction of the minor axis, and ω is the angular velocity of Chlamydomonas. Since the motion of Chlamydomonas satisfies the formula of ellipsoid in Stokes flow[4], for a given combination of velocities and angular velocities, the resultant force and moment of Chlamydomonas can be obtained by superposition:

$$f_x = 6\pi\mu a C_{fx} v_x \tag{S9}$$

$$f_y = 6\pi\mu a C_{fy} v_y \tag{S10}$$

$$F_C = f_C = \sqrt{{f_x}^2 + {f_y}^2} \tag{S11}$$

$$M_{fC} = 8\pi\mu a b^2 C_M \omega \tag{S12}$$

$$M_{fC} = F_C h \tag{S13}$$

Where μ is the viscosity of fluid, a is the major axis, b is the minor axis, F_C is the total tug force of Chlamydomonas, f_C is the the total resistance force of Chlamydomonas, f_x is the component of f_C in the direction of the major axis, f_y is the component of f_C in the direction of the minor axis, M_{fC} is the total resistance moment of Chlamydomonas, and h is the moment arm. Moreover, C_{fx}, C_{fy}, and C_{Mf} are the correlation coefficients with the shape of the ellipsoid:

$$C_{fx} = \frac{8}{3} e^3 \left[-2e + (1 + e^2) \ln \frac{1+e}{1-e}\right]^{-1} \tag{S14}$$

$$C_{fy} = \frac{16}{3} e^3 \left[2e + (3e^2 - 1) \ln \frac{1+e}{1-e}\right]^{-1} \tag{S15}$$

$$C_M = \frac{4}{3} e^3 \left(\frac{2-e^2}{1-e^2}\right) \left[-2e + (1 + e^2) \ln \frac{1+e}{1-e}\right]^{-1} \tag{S16}$$

$$e = \sqrt{1 - \frac{b^2}{a^2}} \tag{S17}$$

In *a* typical rotational motion, the Chlamydomonas showed a circular trajectory with displacement velocity of 25.53±5.04 μm/s and angular velocity of 5.61±1.01 rad/s (Fig. S2C-E). The total tug force of rotational motion Chlamydomonas was 12.35±2.15 pN and the moment arm was 4.67±1.01 μm (Fig. S2F). In a typical straight motion, the Chlamydomonas showed a near rectilinear trajectory with displacement velocity of 41.55±7.63 μm/s and angular velocity of -0.14±1.54 rad/s (Fig. S2G-I). The total tug force of straight motion Chlamydomonas was 12.62±2.34 pN and the moment arm was 0.09±0.05 μm (Fig. S2J).

Numerical simulation of fluid dynamics

The 2D fluid dynamics of the CI-Robot under different driving forces were established, meshed, and simulated by COMSOL Multiphysics 6.1. The multi-physics simulation of fluid-structure interaction includes *k-ε* turbulent flow module, solid mechanics module and moving mesh deforming domain module. Where the calculation domain of the straight motion was 100 mm × 20 mm rectangle region, and the calculation domain of the rotational motion was Φ50 mm round region. The wall around calculation domain were open boundaries and set 0 Pa press point constraint at the corner of the wall. In numerical solution, the fluid resistance and resistance moment were obtained by the surface integral of the stress per unit area in the corresponding projection direction:

$$f_p = \oint_S p \, \mathrm{d}S \tag{S18}$$

$$f_k = \oint_S k \, \mathrm{d}S = \oint_S \frac{\rho u_\tau u^T}{u^+} \, \mathrm{d}S \tag{S19}$$

$$M_p = \oint_S \left(f_{px} y + f_{py} x\right) \mathrm{d}S \tag{S20}$$

$$M_k = \oint_S \left(f_{kx} y + f_{ky} x\right) \mathrm{d}S \tag{S21}$$

$$f = f_p + f_k \tag{S22}$$

$$M = M_p + M_k \tag{S23}$$

Where f is the fluid resistance, M is the fluid resistance moment, p is the fluid pressure, k is the unit area viscous stress, S is the contact surface between CI-Robot and fluid, ρ is the fluid density, u_τ is the friction velocity, u^T is the tangential velocity, u^+ is the tangential dimensionless velocity, x and y are the projected lengths of axis for the distance from the model surface to the center of rotation, and the subscript represents the component of the corresponding physical quantity.

Factors affecting the rotation and straight speed of CI-Robot

To verify universality, five kinds of fuel with different surface tension, different concentrations ethanol and different viscosity solution were used to study the effect of different driving conditions on the rotational motion. The surface tension of the fuel directly determines the velocity of movement. Therefore, the combination of surface tension differences between fuel and solution could make the CI-Robot obtain a different rotation speed (Fig. S14A). The combination of surface tension between different fuels and solutions provided more options for the range of fuel and the application in specific solution situations. In addition, using different ethanol concentrations could obtain different rotation speeds, and the higher the concentration the faster the rotation (Fig. S14B). What is worth mentioning is that the CI-Robot can still drive even when the ethanol concentration is 10 %, which provides convenience for the long-term movement. On the other hand, the viscosity of solution affected the friction coefficient, the higher the viscosity, the slower the rotation (Fig. S14C). After the viscosity surpass 3 mPa·s, the rotation of the CI-Robot becomes difficult, indicating the movement environment requirements of the CI-Robot.

Similarly, we studied the effect of different driving conditions on the straight motion. In the average straight speed using a variety of organic reagents as fuel, the CI-Robot can get the most fast straight speed when using acetone as fuel due to its lowest surface tension (Fig. S18A). As the concentration of ethanol in the fuel increases, the CI-Robot traveled faster (Fig. S18B). When the ethanol concentration was between 40% and 80%, the straight speed of CI-Robot changed gently, and a plateau period appears. It showed that the straight motion was not sensitive to changes in ethanol concentration at this time, which is also the reason for the CI-Robot runs at a constant speed in the T4 stage. In addition, even if the ethanol concentration was as low as 10%, the CI-Robot could still achieve drive at a speed of 20 mm/s, which provides convenience for long time movement. As the solution viscosity increased, the fluid's frictional resistance grew, slowing the CI-Robot's straight-line speed (Fig. S18C). When viscosity rose from 1.5 mPa·s to 3 mPa·s, the straight-line

speed rapidly declined. However, beyond 3 mPa·s, the straight-line speed became less sensitive to viscosity. Even at a viscosity of 6 mPa·s, the CI-Robot was still able to move.

Numerical simulation of dimensionless repulsive force in collective motion

The 2D fluid dynamics of two CI-Robots collective motion were established, meshed, and simulated by COMSOL Multiphysics 6.1. The multi-physics simulation of fluid-structure interaction includes *k*-*ε* turbulent flow module, diffusion module, solid mechanics module and moving mesh deforming domain module. Where the calculation domain was Φ50 mm round region. The wall around calculation domain were open boundaries and set 0 Pa press point constraint at the corner of the wall. In the numerical solution, we get the distribution of fluid velocity (u) and ethanol concentration ($C_{Ethanol}$) in the middle water area between the two CI-Robots. Therefore, dimensionless repulsive force can be derived:

$$F_0 = \oint_B \gamma \, \mathrm{d}B \approx \gamma B_0 \tag{S24}$$

$$F_m = \oint_B (\gamma - \gamma_s) \, \mathrm{d}B \approx (\gamma - \overline{\gamma_s}) B_0 \tag{S25}$$

$$F_u = \oint_B 0.5\rho u^2 \, \mathrm{d}B \approx 0.5\rho \bar{u}^2 B_0 \tag{S26}$$

Where F_0 is the total tension of the CI-Robot in water, γ is the surface tension of water, B is length of the contact between water and CI-Robot, B_0 is the equivalent length of the contact between water and CI-Robot which is hard to calculated, γ_s is the surface tension around the contact which could calculated by equation (9), $\overline{\gamma_s}$ is the average surface tension around contact, ρ is the density of aqueous solution, and $\bar{u}$ is the average fluid velocity. By combining equation (S24)-(S26), B_0 can be eliminated：

$$\frac{F_m}{F_0} = \frac{(\gamma - \overline{\gamma_s})}{\gamma} \tag{S27}$$

$$\frac{F_u}{F_0} = \frac{0.5\rho \bar{u}^2}{\gamma} \tag{S28}$$

Programed locomotion and multifunctional execution of CI-Robot in complex scene

The small size, rapid movement, and complex coupled swimming capabilities make the bioinspired robot highly promising for a variety of applications, particularly in programmable complex path planning[5] and cargo handling[6]. To showcase the robot's programmable complex path planning, we designed an experimental setup consisting of a circular pipe tank connected to two rectangular water tanks (Fig. S22, Movie S6). The circular pipe section was a semi-circle with a diameter of φ=14 mm, designed to simulate a typical pipe connection. After filling with fuel, the CI-Robot was first placed on the left wide body of water to perform a self-driven rotating motion. We set a gradient navigation magnetic field in the right direction within the left water area and at the entrance of the circular pipeline, and another gradient navigation magnetic field in the left direction within the right water area and at the entrance of the circular pipeline. The two navigation magnetic fields were withdrawn immediately after the CI-Robot entered the circular channel. When the CI-Robot approached the navigation magnetic field, its head direction was adjusted and maintained. At this point, the CI-Robot's head tilted slightly downward, and fuel was released through the rear outlet under the influence of gravity to achieve straight movement. After entering the annular pipe in the lower right part, where no navigation magnetic field was present, the CI-Robot adjusted its position using its own buoyancy. The flagellar channel on one side floated up and released fuel, causing a rotating motion. Due to the boundary conditions of the annular pipe, the CI-Robot rolled along the surface of the pipe. Upon reaching the water entrance on the right, the CI-Robot continued to enter the loop pipe on the upper left under magnetic navigation control, maintaining its rolling motion. Ultimately, the complex path movement around the circular pipe was successfully realized with the aid of the preset external magnetic field navigation system.

Besides the magnetic navigation system, the autonomous movement of the CI-Robot in the maze was realized by utilizing the fluid reaction force generated by the boundary conditions. The internal mechanism was that when the CI-Robot moved through the narrow channel, the surface tension of the fluid created a

highly curved water surface at the channel boundary, which forced the CI-Robot to move away from the surface of the channel. When the CI-Robot reached the boundary gap, it autonomously selected the gap without surface tension, due to the presence of surface tension at the boundary. Therefore, as the CI-Robot moved through the maze, it autonomously chose the gap with low surface tension, selecting the optimal path to enter the center of the maze. As shown in Fig. S23, we prepared a circular labyrinth water tank with a width of 15 mm, designed using 3D printing with strong hydrophobic resin materials. When the CI-Robot was placed in the outermost channel of the circular maze, it moved in a rotating and rolling state. Upon reaching a gap, the CI-Robot was pushed by the surface tension of the channel and could autonomously be pushed into the gap, entering the second circle of the channel. In this process, without human intervention, the robot ultimately chose the path with low surface tension to reach the center of the maze.

To further investigate the ability of the CI-Robot to avoid obstacles in complex water scenes, we constructed a tank with an array of cylinders. The narrowest distance from the cylindrical surface in the tank was 12 mm, while the maximum width of the CI-Robot was about 11.65 mm from the end of the two flagella. At this limit width, we evaluated whether the microrobot could bypass the small cylinders. As shown in Fig. S24, when the CI-Robot was initially placed in the cylindrical array area, it could perform rotational motion, but the flagella collided with the cylindrical array. As a result, it only displayed self-driven rotational motion within the restricted area and could not bypass the cylinder. With magnetic navigation, the CI-Robot was precisely controlled to perform directional obstacle-avoidance movements within the column array intervals to reach the next interval. After the magnetic field was removed, the CI-Robot continued to rotate in the restricted area near the four small cylinders. The results showed that the CI-Robot could not avoid obstacles in the narrow area near its maximum width on its own, but it was able to plan a path to avoid obstacles when guided by the magnetic field. Furthermore, we have achieved the fixed-point cargo handling capabilities of CI-Robot (Fig. S25, Movie S6). The outlet of the flagella fuel channel of the CI-Robot was blocked by using

a photo responsive gel, and a small black disc was glued as a model of small cargo. Controlled by a preset magnetic field path, the CI-Robot moved from the upper right side of the array column tank along a specified route to the column marked with a blue five-pointed star. The CI-Robot was then stimulated by a long-range near-infrared laser, causing the photoresponsive gel to discharge and the small black disc to detach. After placing the cargo in the designated area, the CI-Robot continued along the planned path to reach the final location.

Supplementary Figures

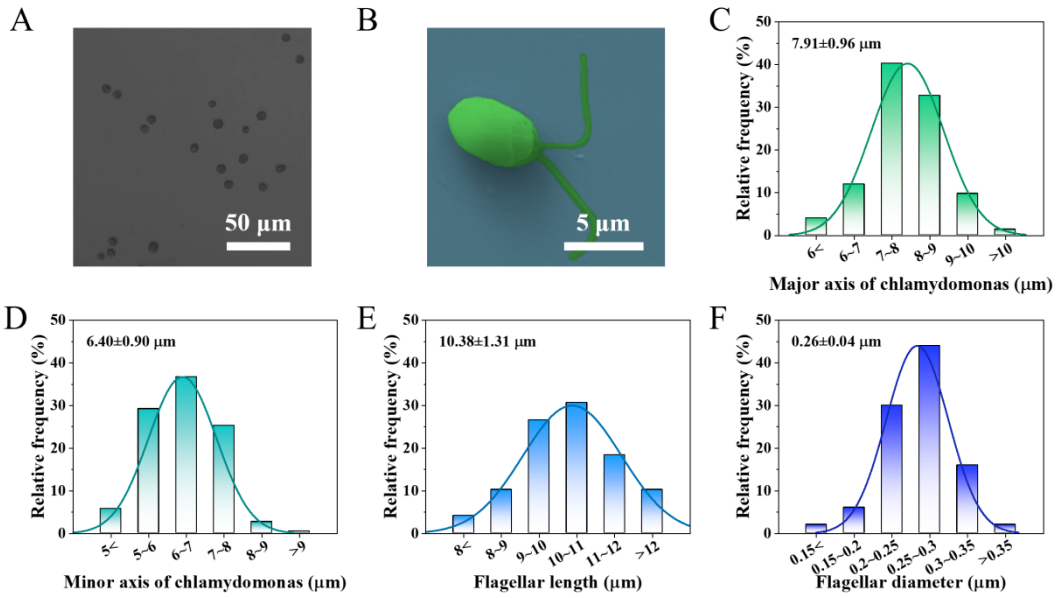

Fig. S1 The morphology characterization of Chlamydomonas. (**A**) Micrograph image and (**B**) typical SEM image of Chlamydomonas. (**C**) Major axis and (**D**) minor axis distribution of Chlamydomonas. Statistics of 300 Chlamydomonas. (**E**) Length and (**F**) diameter distribution of Chlamydomonas flagellar. Statistics of 50 Chlamydomonas.

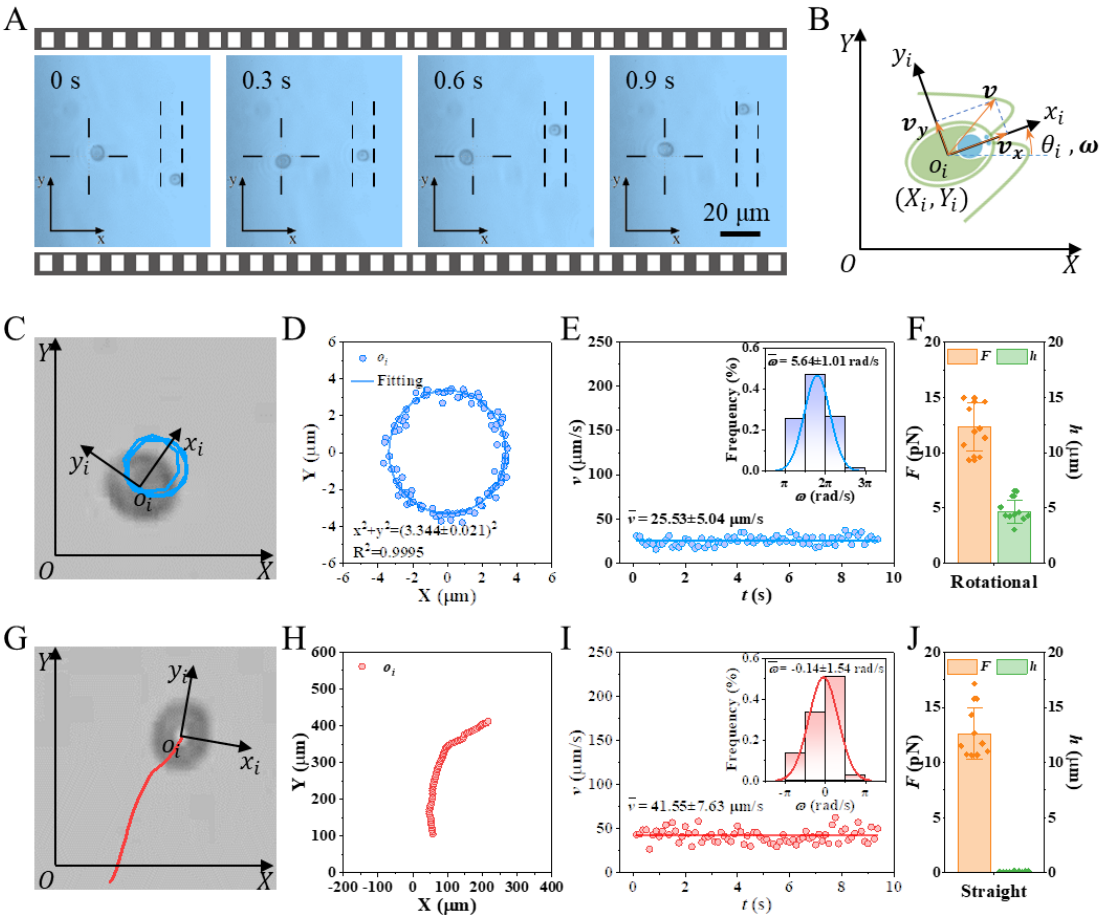

Fig. S2 The locomotion behavior of Chlamydomonas. (**A**) Rotational and straight motion of Chlamydomonas. See **Movie S1**. (**B**) Schematic of the Chlamydomonas' locomotion showing the video frame of reference (*O*-*XY*) and the Chlamydomonas' body frame of reference (o_i-x_iy_i). The video frame of reference is stationary, and the origin of the Chlamydomonas' body frame of reference is established at the center of their body. The Chlamydomonas' body frame of reference translates with velocity (v) and rotates with angular velocity (ω). (**C**) The spatiotemporal evolution of Chlamydomonas rotational motion positions. The blue line is the locus of the body center of the rotational motion of Chlamydomonas. (**D**) The locus coordinates of the body center in a typical rotational motion. (**E**) The instantaneous velocity and angular velocity of Chlamydomonas in a typical rotational motion. (**F**) Statistics of the total tug force and the moment arm of ten groups of rotational motion Chlamydomonas. (**G**) The spatiotemporal evolution of Chlamydomonas straight motion positions. The blue line is the locus of the body center of the straight motion of Chlamydomonas. (**H**) The locus coordinates of the body center in a typical straight motion. (**I**) The instantaneous velocity and angular velocity of Chlamydomonas in a typical straight motion. (**J**) Statistics of the total tug force and the moment arm of ten groups of straight motion Chlamydomonas.

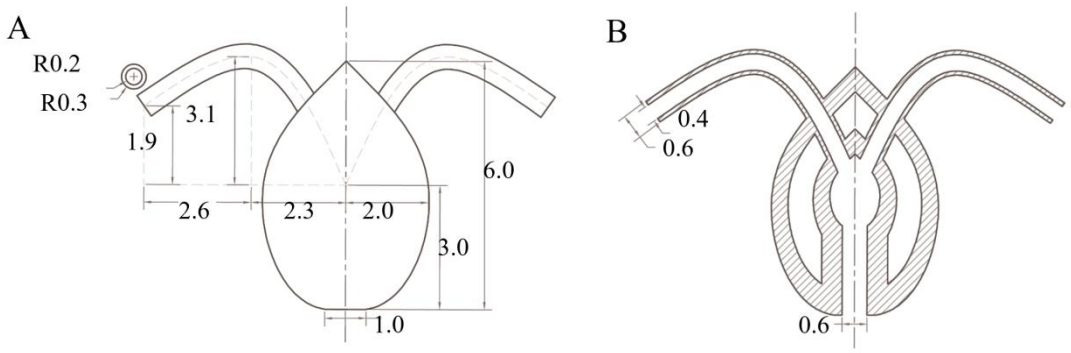

Fig. S3 Design drawing of CI-Robot. (**A**) The appearance size design of CI-Robot. (**B**) The cutaway view of CI-Robot.

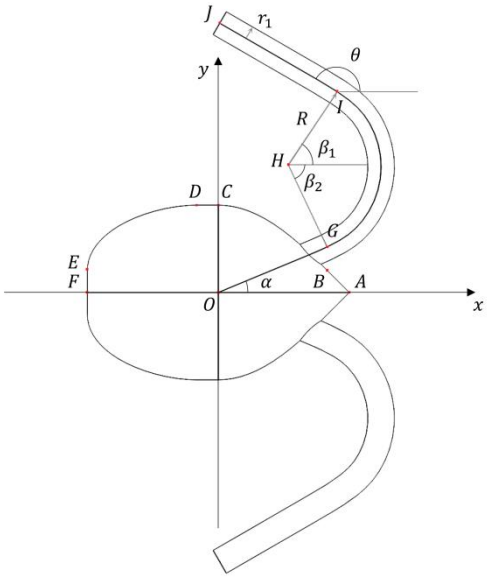

Fig. S4 The flagella optimization of CI-Robot.

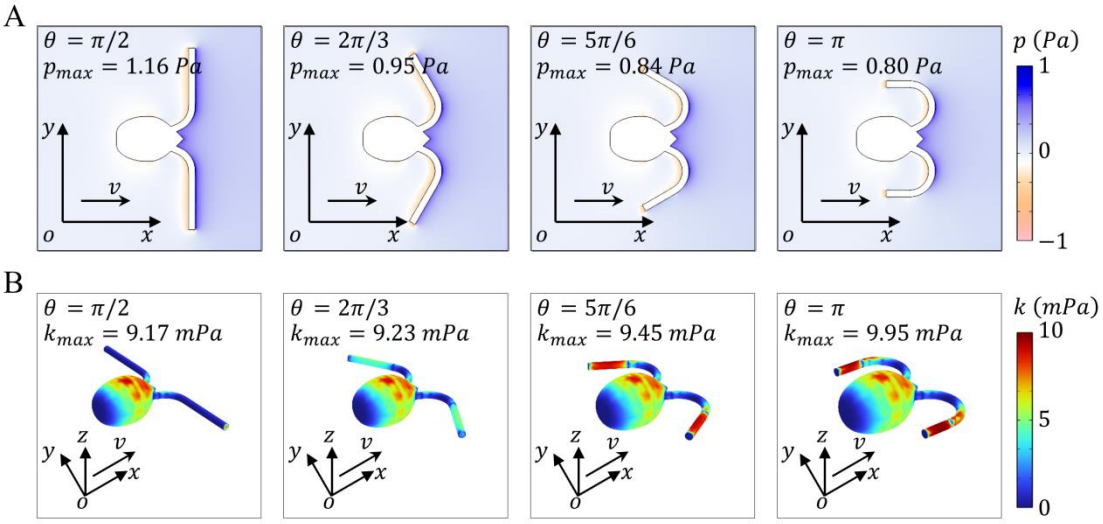

Fig. S5 The changes in fluid resistance of CI-Robot with increasing of flagella epitaxial angle (θ). (**A**) Pressure distribution, (**B**) viscous stress distribution.

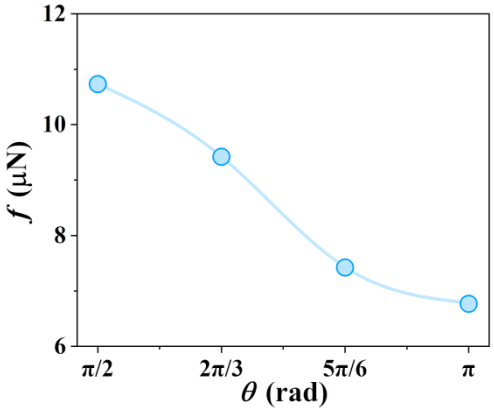

Fig. S6 The fluid resistance in the direction of incoming flow at different θ.

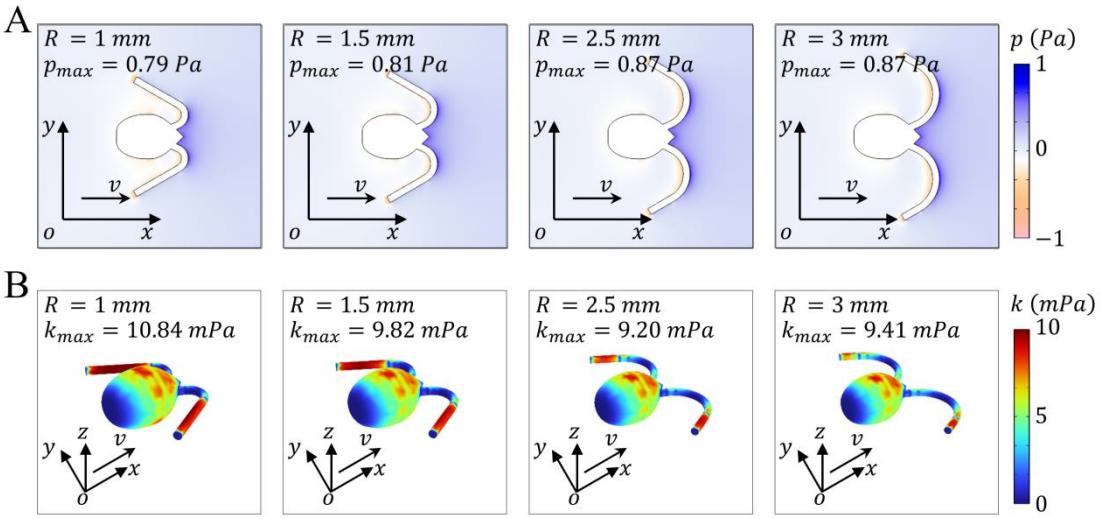

Fig. S7 The changes in fluid resistance of CI-Robot with increasing of flagella bending radius (*R*). (**A**) Pressure distribution, (**B**) viscous stress distribution.

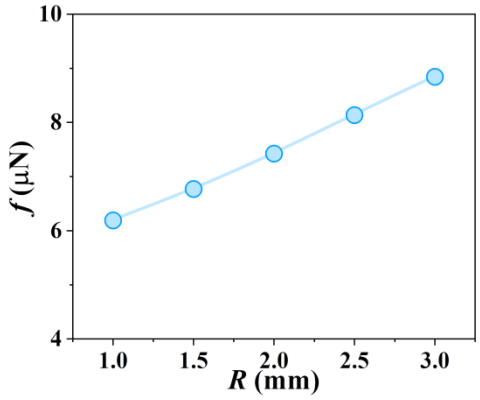

Fig. S8 The fluid resistance in the direction of incoming flow at different *R*.

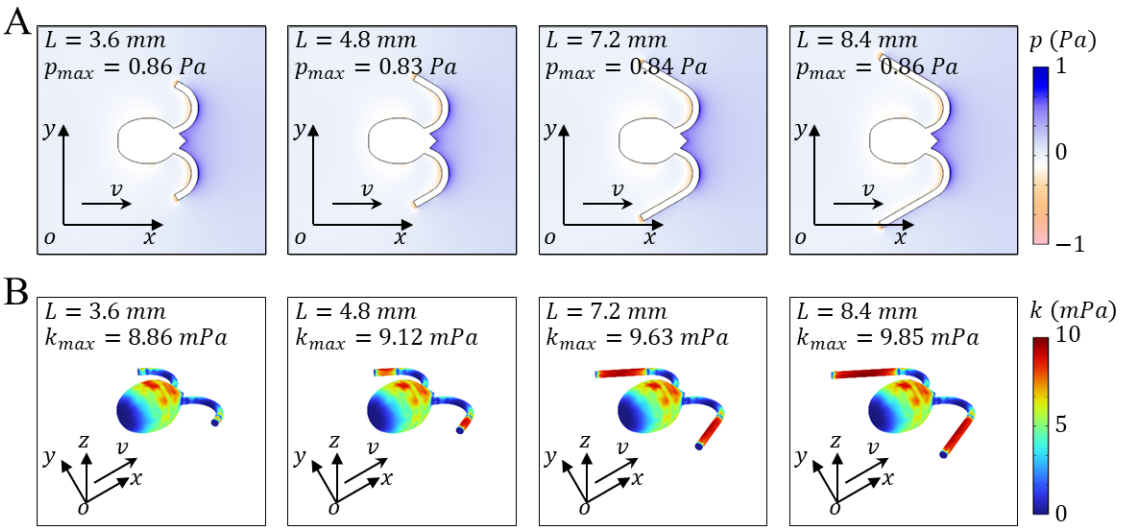

Fig. S9 The changes in fluid resistance of CI-Robot with increasing of flagella length (*L*). (**A**) Pressure distribution, (**B**) viscous stress distribution.

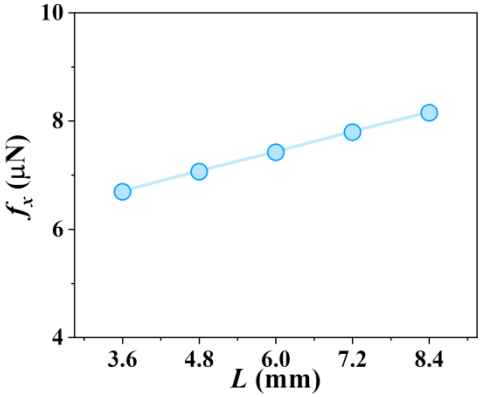

Fig. S10 The fluid resistance in the direction of incoming flow at different *L*.

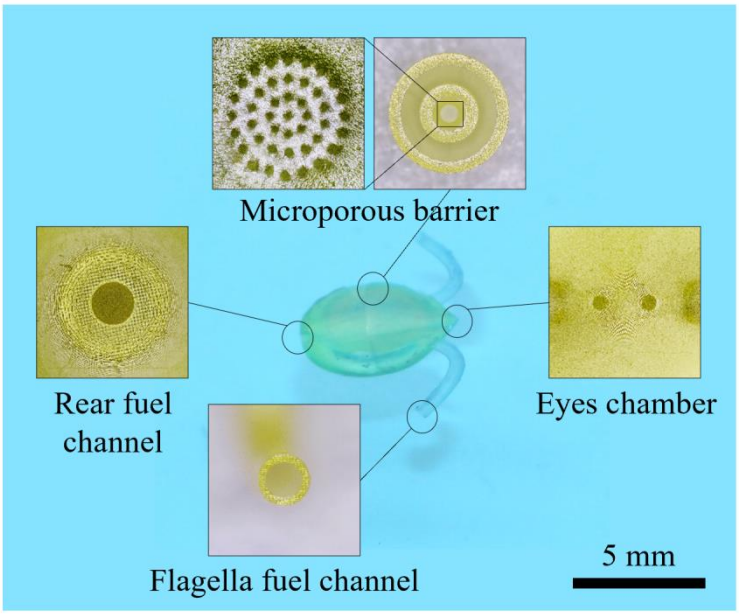

Fig. S11 The optical image of assembled CI-Robot on the water. The insert images are micrographs of various parts of CI-Robot. The CI-Robot is composed of flagella fuel channel, rear fuel channel, microporous barrier, magnetic eyes chamber, buoyancy chamber and fuel storage chamber.

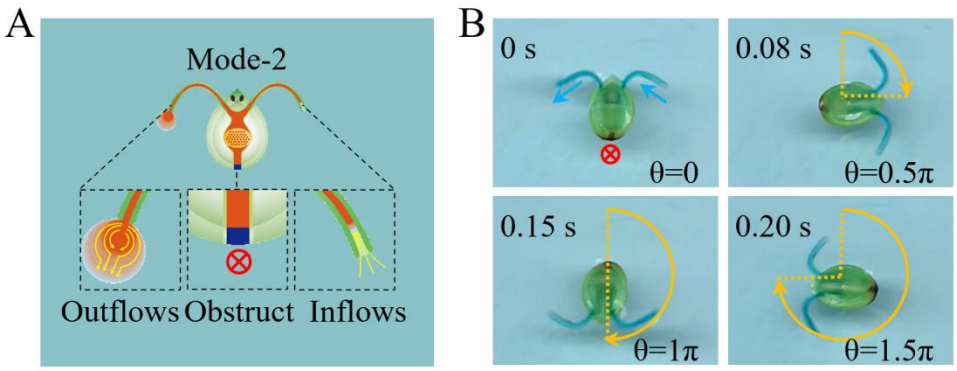

Fig. S12 Mode-2 of rotational CI-Robot. (**A**) Schematic of Mode-2. (**B**) Motion sequence of Mode-2.

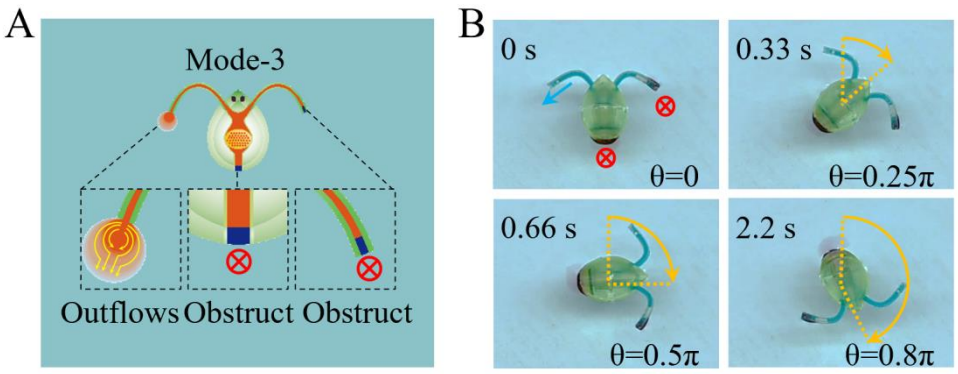

Fig. S13 Mode-3 of rotational CI-Robot. (**A**) Schematic of Mode-3. (**B**) Motion sequence of Mode-3.

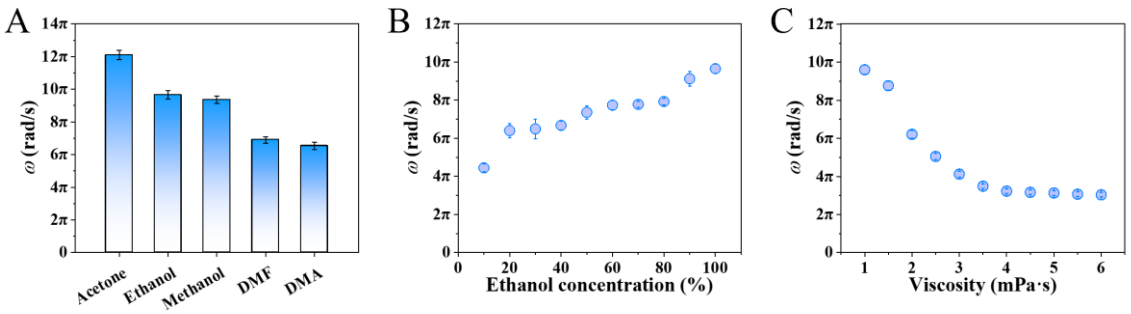

Fig. S14 The influencing factors on CI-Robot in rotational mode. (**A**) The max angle velocity of CI-Robot driven by different surface tension solutions. (**B**) The max angle velocity of CI-Robot driven by different concentration of ethanol. (**C**) The max angle velocity of CI-Robot driven by ethanol at different viscosity.

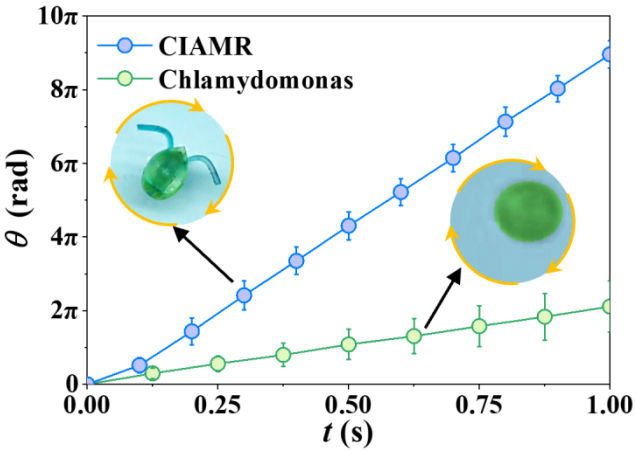

Fig. S15 The comparison of rotational motion performance between Chlamydomonas and CI-Robot driven by 100% ethanol fuel with mode-1 in aqueous solution.

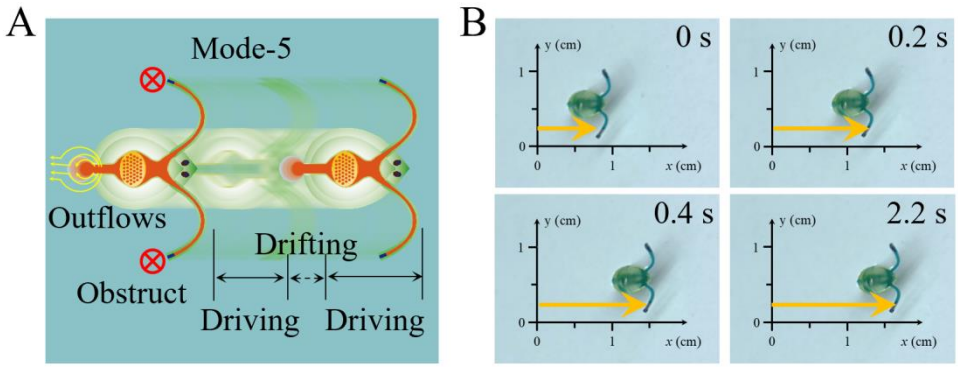

Fig. S16 Mode-5 of straight CI-Robot. (**A**) Schematic of Mode-5. (**B**) Motion sequence of Mode-5.

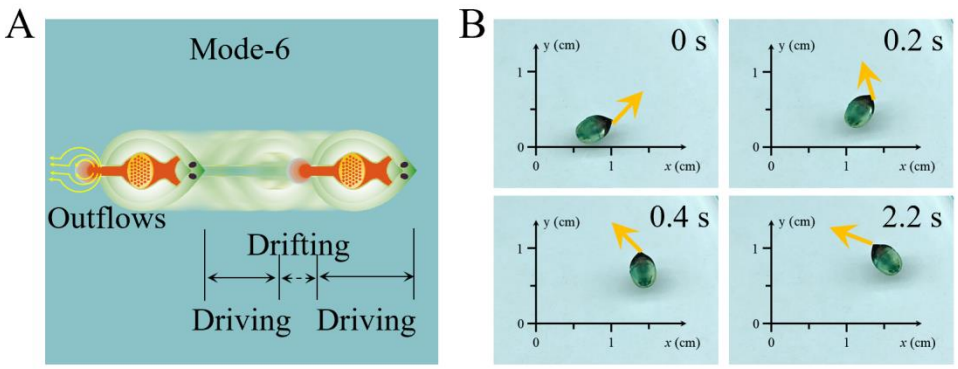

Fig. S17 Mode-6 of straight CI-Robot. (**A**) Schematic of Mode-6. (**B**) Motion sequence of Mode-6.

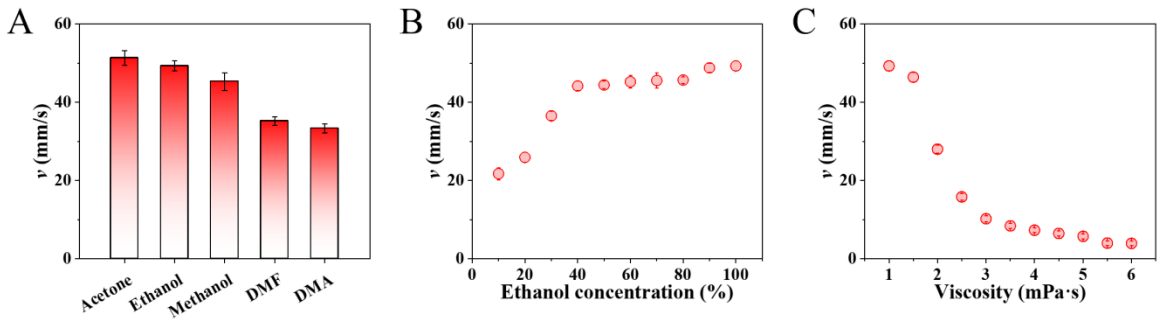

Fig. S18 The influencing factors on CI-Robot in straight mode. (**A**) The max velocity of CI-Robot driven by different surface tension solutions. (**B**) The max velocity of CI-Robot driven by different concentrations of ethanol. (**C**) The max velocity of CI-Robot driven by ethanol at different viscosity.

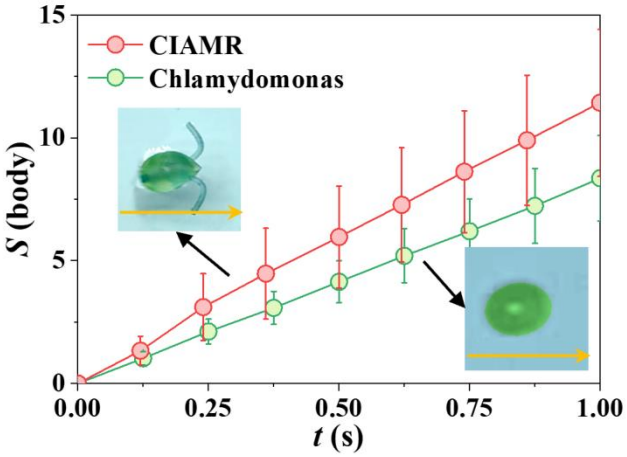

Fig. S19 The comparison of straight motion performance between Chlamydomonas and CI-Robot driven by 100% ethanol fuel with mode-4 in aqueous solution.

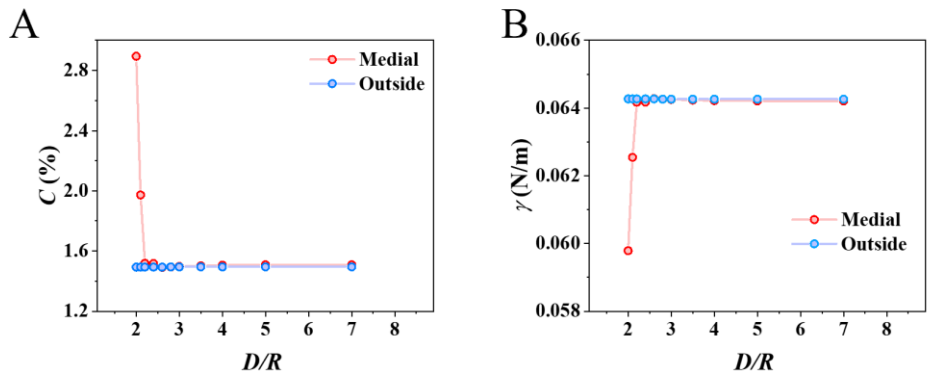

Fig. S20 Ethanol diffusion simulation of CI-Robot in collective rotational mode. (**A**) Ethanol concentration in outer water area and middle water area. (**B**) Surface tension in outer water area and middle water area.

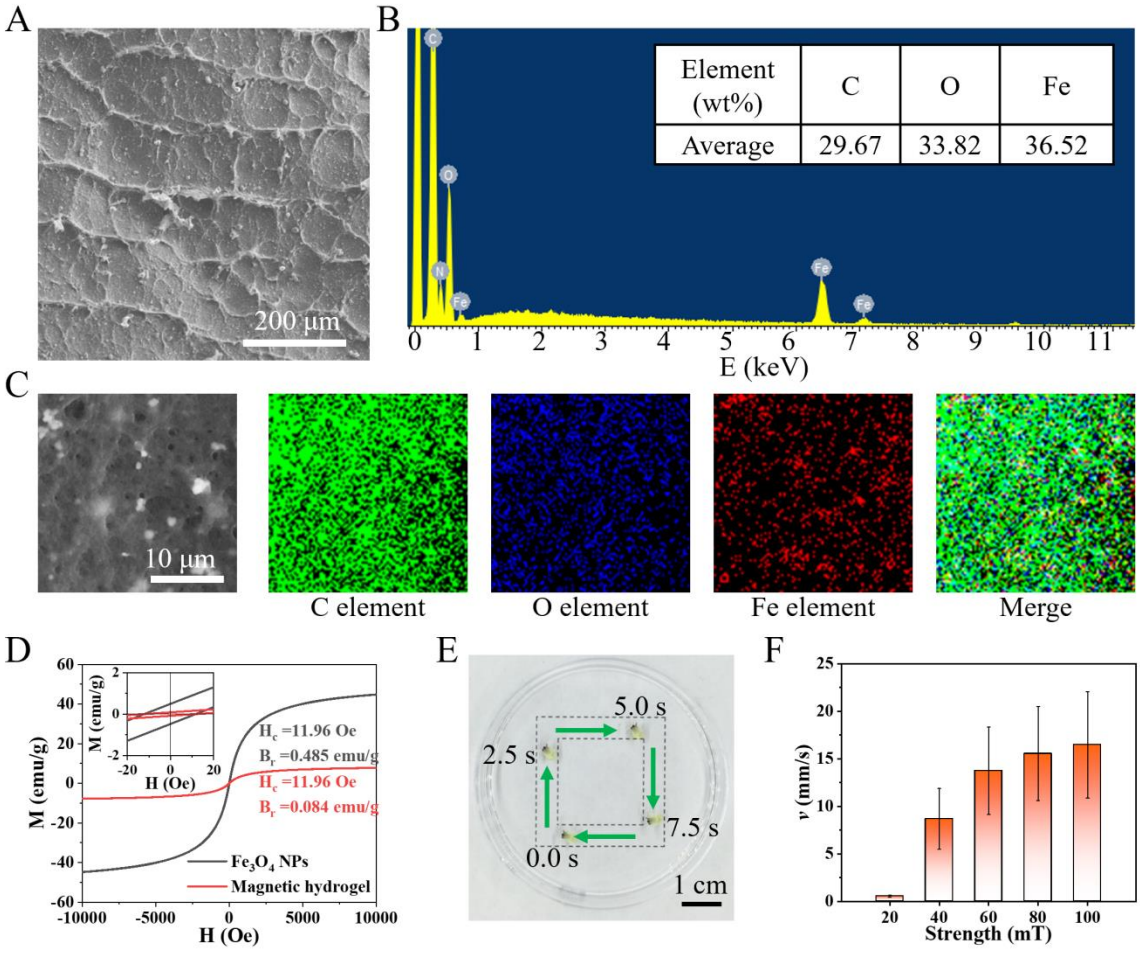

Fig. S21 The characterization of magnetic hydrogel. (**A**) Typical SEM image of magnetic hydrogel. (**B**) EDS mapping of magnetic hydrogel. (**C**) Energy dispersive spectrum of magnetic hydrogel. (**D**) The hysteresis loop of Fe_3O_4 NPs and magnetic hydrogel. (**E**) Magnetic navigation of CI-Robot. (**F**) Velocity of CI-Robot under different magnetic field strength.

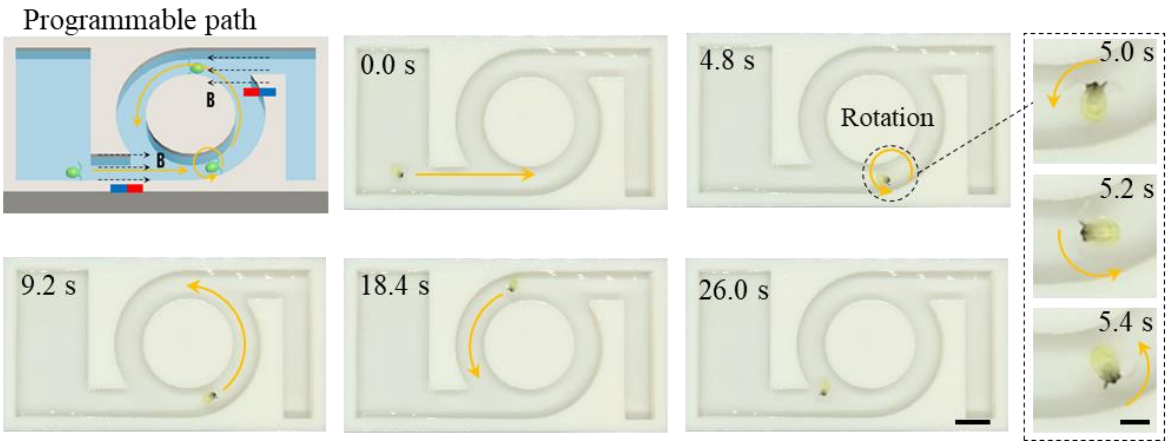

Fig. S22 The circular movement of CI-Robot around cylinder under magnetic guidance.

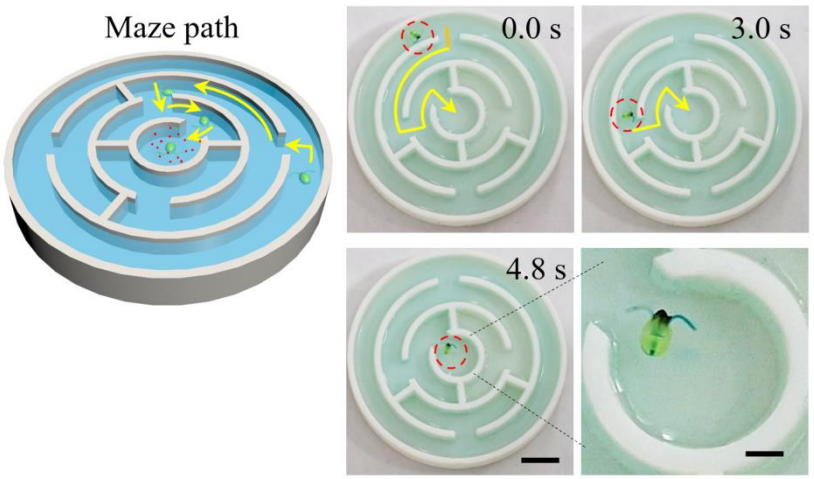

Fig. S23 The maze orientation movement of CI-Robot under surface tension guided.

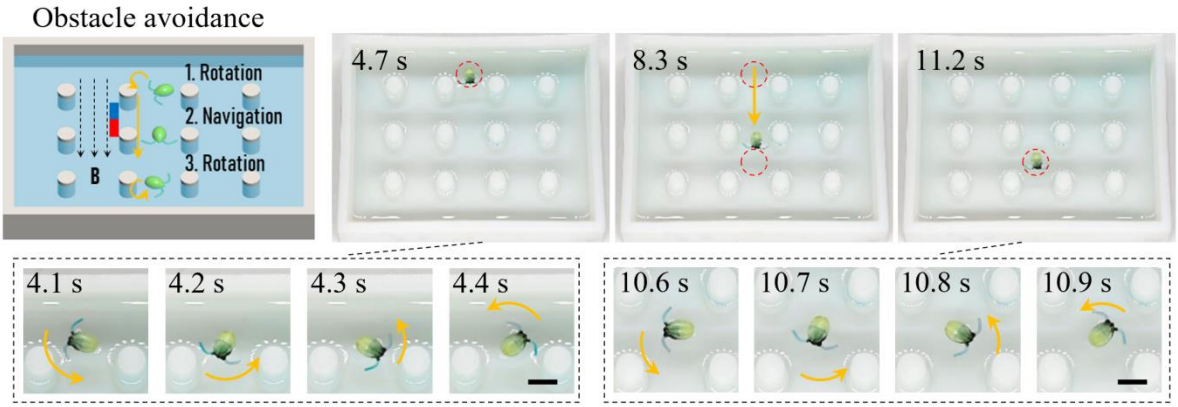

Fig. S24 The obstacle avoidance movement of CI-Robot in cylindrical array flume under magnetic guidance.

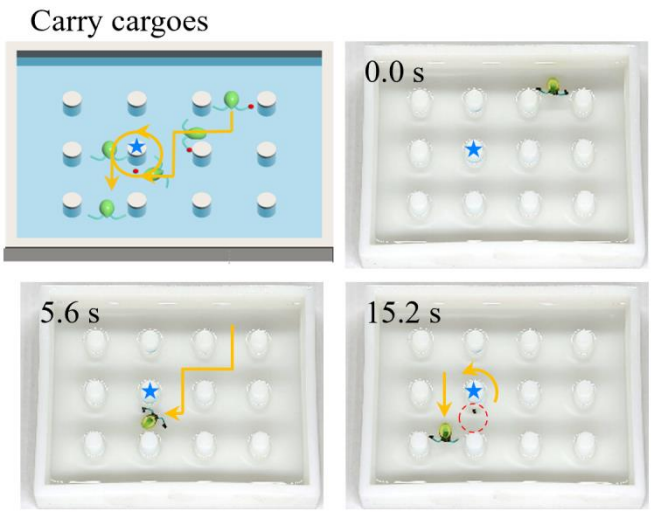

Fig. S25 The fixed-point cargo handling by CI-Robot in cylindrical array flume under magnetic guidance.

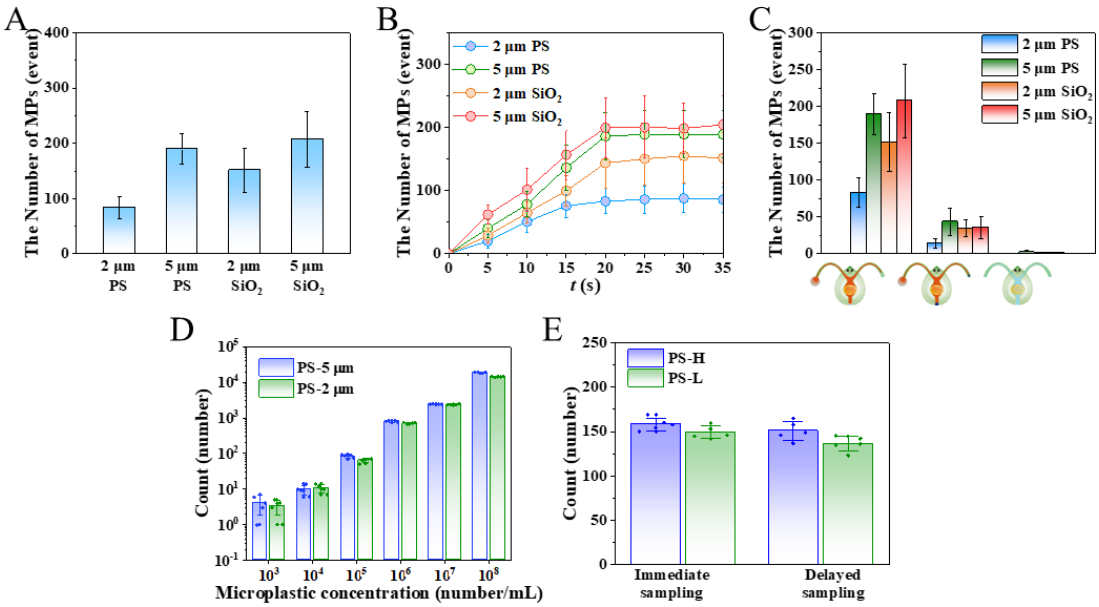

Fig. S26 The microplastic sampling application of CI-Robot in pipeline. (**A**) The sampling number of CI-Robot in 10^5 number/mL microspheres solution with different materials and sizes. (**B**) The sampling number of CI-Robot on different working times. (**C**) The sampling number of CI-Robot with different motion modes in 10^5 number/mL microspheres solution. (**D**) The sampling number of CI-Robot in different concentrations microspheres solution. (**E**) The sample retention capability of CI-Robot after microsphere sampling.

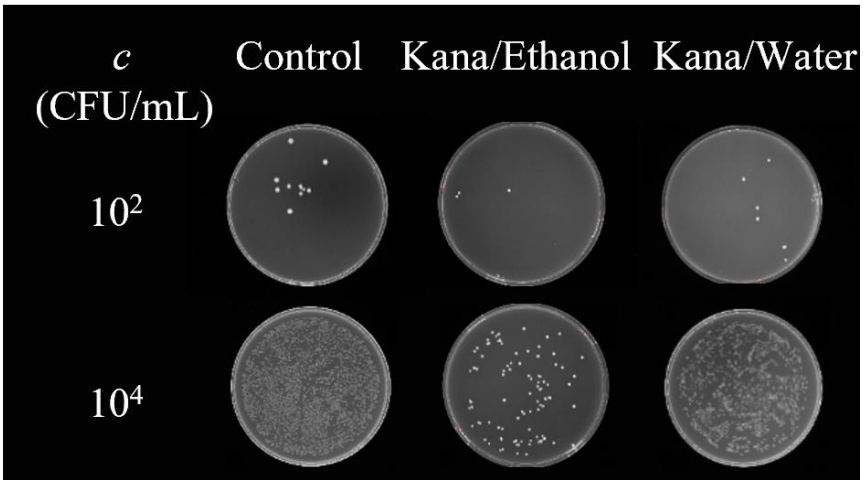

Fig. S27 The flat colony counting after treatment by CI-Robot load with antimicrobial in different fuel.

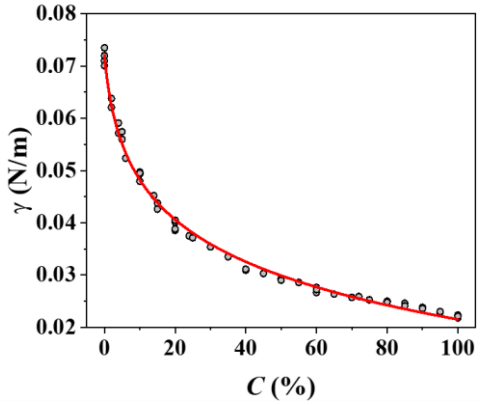

Fig. S28 The surface tension of ethanol solutions with different concentrations.

Movie S1 Chlamydomonas motion captured through microvideo (8.6 fps) and high-speed photography (250 fps).

Movie S2 Robot motion videos with three rotation modes.

Movie S3 Robot motion videos with three straight modes.

Movie S4 Robot motion videos with cluster mode.

Movie S5 Robot cluster movement control videos with magnetic navigation.

Movie S6 Programed locomotion and multifunctional execution of CI-Robot in complex scene.

Movie S7 Application of Chlamydomonas-inspired miniature robot (CI-Robot) in pipeline.

References

1. Li, D. M. *et al.* Controllable and continuous hollow fiber swimmers based on the marangoni effect. *Acs Appl. Mater. Interfaces* **12**, 53503-53509 (2020).
2. Chang, J., Sheng, L. Z., Wei, T. & Fan, Z. J. Molecular diffusion-driven motion in 2D graphene film. *Adv. Funct. Mater.* **28**, 1707053 (2018).
3. Geyer, V. F., Jülicher, F., Howard, J. & Friedrich, B. M. Cell-body rocking is a dominant mechanism for flagellar synchronization in a swimming alga. *Proc. Natl. Acad. Sci. U. S. A.* **110**, 18058-18063 (2013).
4. Song, Y. *et al.* Multiple forces facilitate the aquatic acrobatics of grasshopper and bioinspired robot. *Proc. Natl. Acad. Sci. U. S. A.* **121**, 2313305121 (2024).
5. Ke, X., Yong, H., Xu, F., Ding, H. & Wu, Z. Stenus-inspired, swift, and agile untethered insect-scale soft propulsors. *Nat. Commun.* **15**, 1491 (2024).
6. Piñan Basualdo, F. N., Bolopion, A., Gauthier, M. & Lambert, P. A microrobotic platform actuated by thermocapillary flows for manipulation at the air-water interface. *Sci. Robot.* **6**, 3557 (2021).